QUIET DRONES
Second International e-Symposium
on
UAV/UAS Noise
27th to 30th June 2022

Measurement of sound emission characteristics of quadcopter drones under cruise condition

Gert Herold[*], **Paul Testa, Jan Foerster, Maarten Uijt de Haag, Ennes Sarradj**

Technische Universität Berlin

Summary

Quadcopter drones have distinctive sound emission characteristics, which also depend on their mode of operation. While determining these characteristics is of interest in different contexts, this proves particularly challenging when the mode of operation involves movement of the drone.

In this contribution, a method for characterizing the in-flight sound radiation in terms of sound power and directivity is applied to three different drone configurations flying at different speeds. Based on microphone array measurements, the trajectory of the drone during its flight through the array is reconstructed. The estimated flight path is then used to de-dopplerize the measured signals and determine the directivity based on the time-dependent relative angle of radiation from the drone to the microphones.

The exemplary evaluations include the calculation of sound power spectra and directivity factors. Current limitations of the method are highlighted and ways to overcome them are discussed.

---

[*]Corresponding author: gert.herold@tu-berlin.de

1. Introduction

Multicopter drones are more and more becoming part of our everyday life. As the number of applications for such devices increases, so does the interest in researching their noise emissions and the effects on humans [1], as well as in taking regulatory measures to ensure the well-being of the general public [2].

While for the individual, it is the sound *immission* that counts, i.e. the noise to which they are exposed, a description of the sound *emission* is more useful, for example, when simulating the noise exposure based on different scenarios or when setting permit limits.

For stationary sources, methods for determining sound emission characteristics by placing micro-phones around the object are widely used [3]. While many drones can remain stationary in hover mode, cruise flight also constitutes a typical mode of operation that can be associated with unique sound generation, e.g. with specific tonal components exhibiting a strong directivity.

In the following, a novel method for characterizing sound emissions by taking into account a relative movement between the object and the sensors is applied to multiple drone fly-bys. The basis of the multi-step processing are microphone array measurements, which are evaluated to both reconstruct the flight path and determine the directed sound emissions.

2. Materials and methods

2.1 Measured drones

Figure 1: Drone configurations D1 (left) and D3 (right). Configuration D2 is identical to D3 with a different set of propellers.

Measurements were done with two different consumer quadcopter drones (depicted in Fig. 1). Configuration "D1" has a width of about 38 cm and a height of about 9 cm when viewed from the front. Configurations "D2" and "D3" are the same drone with a different set of propellers, with a width of about 47 cm and a height of 8 cm. Table 1 summarizes several drone-specific parameters.

All drones were steered manually, with the maneuvers consisting of acceleration after hovering, then straight flight and deceleration. For D2 and D3, measurements with two different speeds are evaluated, with an appended "s" denoting a lower flight speed and "f" a higher speed.

Table 1: Drone dimensions and parameters.

	D1	D2	D3
weight	500 g	750 g	
diagonal rotor axes distance	289 mm	335 mm	
dimensions ($l \times w \times h$)	33 cm × 38 cm × 9 cm	43 cm × 47 cm × 8 cm	
blades per rotor	3	2	
propeller diameter	154 mm	210 mm	216 mm

2.2 Measurement setup

The measurements were done in a fully anechoic room at TU Berlin. Figure 2 shows the general setup. Sound pressures were recorded synchronously with 96 channels distributed over two arrays. The plate array on the side features 32 flush-mounted microphones in a spiral arrangement with a diameter of about 1.5 m. 64 microphones are evenly distributed in a ring with a diameter of 2.1 m.
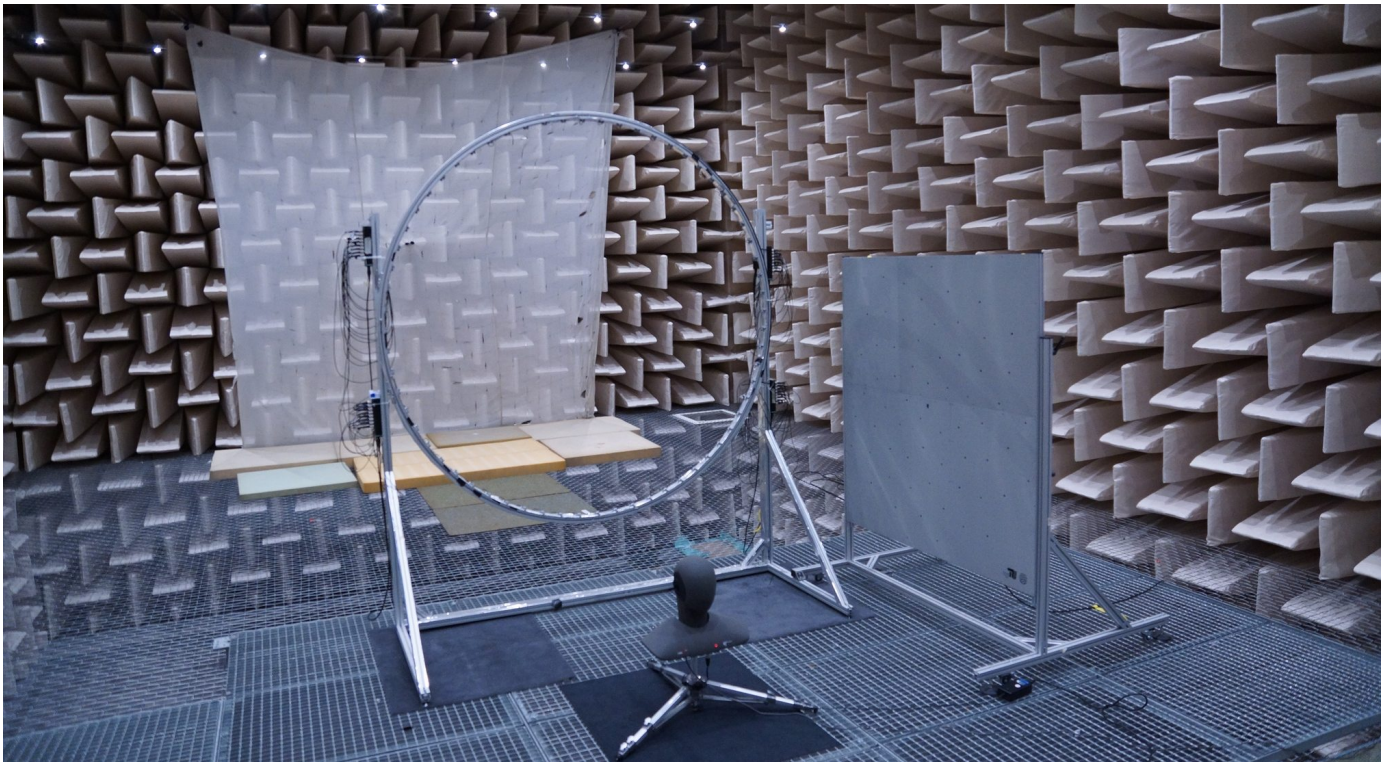

Figure 2: Measurement setup with the two arrays (artificial head not used here). View in flight direction (along the z axis).

The drones' flight paths start approximately 4 m before the ring, on the side of the room where the plate array and the artificial head are positioned. The drones are steered to fly through the ring center and stop approximately 4 m after passing the ring. Due to the spatial constraints in the anechoic room, the drones are not operated at a constant speed during the full 8 m flight path, which includes portions of acceleration and deceleration. In addition, dealing with the wire mesh floor proved to be a challenge for the drone's internal position stabilization, which made it difficult to keep the drone stable in a given hover position.

The microphones of the plate array were used exclusively for the flight path reconstruction. The ring array was used for the emission characterization. This is described in the following section.

2.3 Signal processing

The objective of the measurements is to achieve a characterization of the directed sound emission of the moving drones. An advantage of measuring moving drones is that the signals recorded with stationary sensors describe the sound immission from varying incident angles. If the source position is known, emission characteristics can be derived by compensating for the sound propagation through the medium. The necessary steps for this follow the data processing described earlier [4] and shall be summarized here:

1. Reconstruct the flight path of the drone.

2. Compensate for relative distance and motion.

3. Compile a frequency- and direction-dependent description of the emission.

For reconstructing the drone's flight path, signals synchronously recorded with the 32-channel plate array are used. A three-dimensional region where the drone is expected to fly (i. e. a flight corridor) is defined, and Functional Beamforming [5, 6] is used on short-time signal segments to determine the drone's average position by locating the origin of the maximum sound pressure during each time segment. From these coordinates, a coherent trajectory is constructed using a Kalman filter [7]. This part of the processing is described in more in detail in [8]. Important parameters for the trajectory reconstruction are summarized in Table 2.

Table 2: Important parameters for the trajectory detection.

number of microphones	32
sampling rate	51 200 Hz
focus grid ($l_x \times l_y \times l_z$)	2 m × 2 m × 9 m
focus grid resolution	0.05 m
FFT	512 samples
	von Hann window
	50 % overlap
averaging time	0.1 s
beamforming	Functional Bf., $\nu = 8$
	w/o CSM main diagonal
	2.9 kHz ± 150 Hz

With the known trajectory, the influence the drone's motion has on the received signal (i. e. the Doppler effect) as well as the dependence of the sound pressure on the distance r between drone and microphone can be compensated via

$$p_{\text{mic,corr,1 m}}(t) = \frac{r(t)}{(1 - v_{\text{drone,rel}}(t)/c)^2} \cdot p_{\text{mic,meas}}\left(t + \frac{r(t)}{c}\right) . \tag{1}$$

The resulting time signal $p_{\text{mic,corr,1 m}}$ for a specific microphone of the 64-channel ring array is normalized to a distance of 1 m from the drone. The speed of the drone relative to the microphone $v_{\text{drone,rel}}$ can be derived from the trajectory as well. The speed of sound is represented by c in Eq. (1).

Finally, the corrected time signals again are cut into short segments, fourier-transformed, and then collected and averaged according to the current relative azimuth φ and elevation θ between drone and a microphone. For summarizing several emission angles, the radiation direction space is discretized. The drone-centered coordinate system as well as two angle discretizations are shown in Fig. 3.
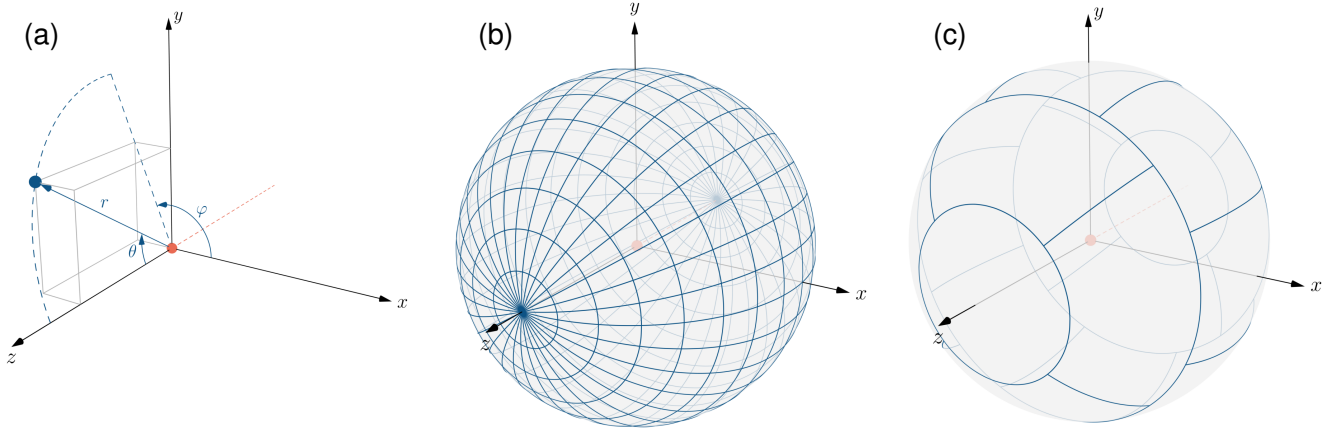
Figure 3: (a) Cartesian and spherical coordinates with the drone (as red dot) at the origin. The dashed red line represents past trajectory. (b) Discretization of sphere into 32×16 sections with equal angle distribution. (c) Discretization of sphere into 18 sections with equal surface area.

The high-resolution angle discretization (Fig. 3b) is used for mapping the 3D radiation characteristics. The equal surface radiation angle discretization (Fig. 3c) is used for calculating the frequency dependent sound power [4]

$$W = \frac{2\,\mathrm{m}^2\,\pi}{9} \sum_{i=1}^{18} \frac{p_{\mathrm{rms},i}^2}{\rho_0 c} \tag{2}$$

and directivity factor

$$Q = \frac{18 \cdot p_{y\text{-}}^2}{\sum_{i=1}^{18} p_{\mathrm{rms},i}^2} \,, \tag{3}$$

where $p_{\mathrm{rms},i}$ is the RMS sound pressure at the i-th segment, $p_{y\text{-}}$ the RMS sound pressure at the segment facing towards negative y, and ρ_0 the air density. Several parameters for the compilation of the directional radiation are summarized in Table 3.

Table 3: Parameters for the directed sample collection.

microphones	64, 2.1 m ring
sampling rate	51 200 Hz
FFT	4096 samples
	von Hann window
	97 % overlap

3. Results

3.1 Flight paths

Figure 4 shows the reconstructed trajectories of the five separately measured cases. As the drones were steered manually, each path is individual and different from the others. As described in Section 2.3, arbitrary paths are accounted for in the signal processing.

However, the path detection assumes that the position of the dominant sound source is representative for the drone's location. In the case of the drones, major sources can be expected to be close
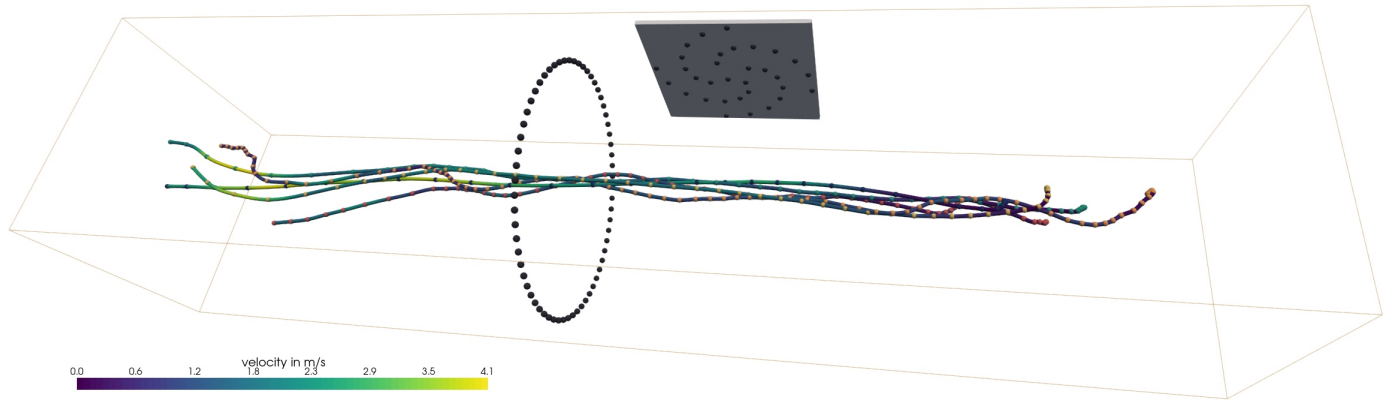
Figure 4: Reconstructed trajectories of the drone flights with velocities. Flight direction from right to left. Colored dots show the respective drone's position every 0.1 s (D1, D2s, D2f, D3s, D3f). Dark gray dots represent microphone positions. The yellow frame indicates the monitored 3D flight corridor.

to the propellers, with the single dominant source possibly switching from one propeller to another throughout the flight. With the propellers of the drones being up to 30 cm apart, this can lead to deviations of the reconstructed from the true path, and to an apparent curved trajectory when the actual cruise flight follows a straight line.

For the calculations done here, the deviation of the position is assumed to be negligible. Furthermore, the orientation of the drone – and with it the direction of the z axis in the coordinate system (Fig. 3a) – is assumed to be constant for the whole flight, with the z axis being oriented from start to the end point of the trajectory.

Table 4: Reconstructed flight paths.

case	max. speed	distance start-end	time start-end
D1	3.9 m/s	7.4 m	3.0 s
D2s	2.3 m/s	7.9 m	8.1 s
D2f	4.0 m/s	8.0 m	4.9 s
D3s	2.1 m/s	6.3 m	5.9 s
D3f	3.5 m/s	7.3 m	4.5 s

In Table 4, the distances between start and end point of the trajectories as well as the elapsed time and the maximum speed in each trajectory are listed. As can be seen in Fig. 4, higher speeds are usually only reached during the second half of the trajectory.

3.2 Directional sound radiation

Figures 5 to 9 show the sound radiation characteristics for octave bands from 500 Hz to 16 kHz for the evaluated cases. Throughout all drone flights and frequency bands, it can be observed that the drones exhibit a distinct directivity, where more sound is emitted towards the ground and upwards than in other directions. This is in line with what is observed from other multicopter drones as well [1].

For configuration D1 (Fig. 5), however, there appears to be a local minimum at $\theta = \pi/2$ in the 500 Hz octave band. This may be a result of only few samples being available for averaging at this angle due to the array geometry and the comparably high flight speed. Furthermore, the 500 Hz octave contains fewer discrete frequencies than the other bands, where the calculated radiation patterns have a smoother characteristic.
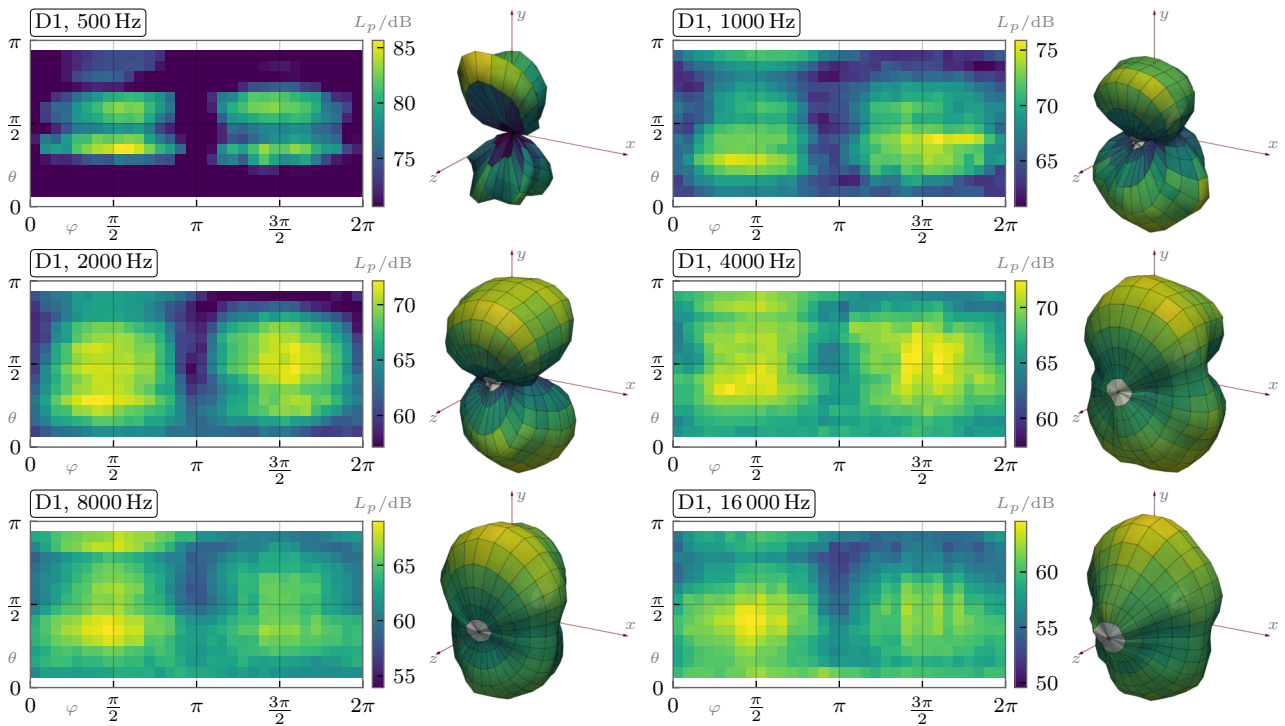

Figure 5: **D1**: Directivity maps for different octave bands. Displayed dynamic up to 15 dB below maximum.

All calculated directivity maps with configurations D2 or D3 exhibit strong levels directed towards the ground and slightly backwards ($\varphi \approx 3\pi/2$, $\theta \gtrsim \pi/2$). These are not caused by actual acoustic phenomena but by pressure fluctuations on the microphones as a result of the downwash created by the drone's propellers. This effect could be mitigated either by adapting the experimental setup (e.g. by adding windscreens to the microphones) or the data processing (e.g. by evaluating a subset of the microphone signals together for filtering out uncorrelated signal portions).

For the octave bands from 2 kHz to 16 kHz, the flow effects are not present. At 4 kHz and above, the D2 and D3 cases exhibit a slightly forward-oriented directivity in addition to the upwards/downwards characteristic. Furthermore, the downward facing lobe is broader than the upward lobe for the octave bands 8 kHz and 16 kHz.
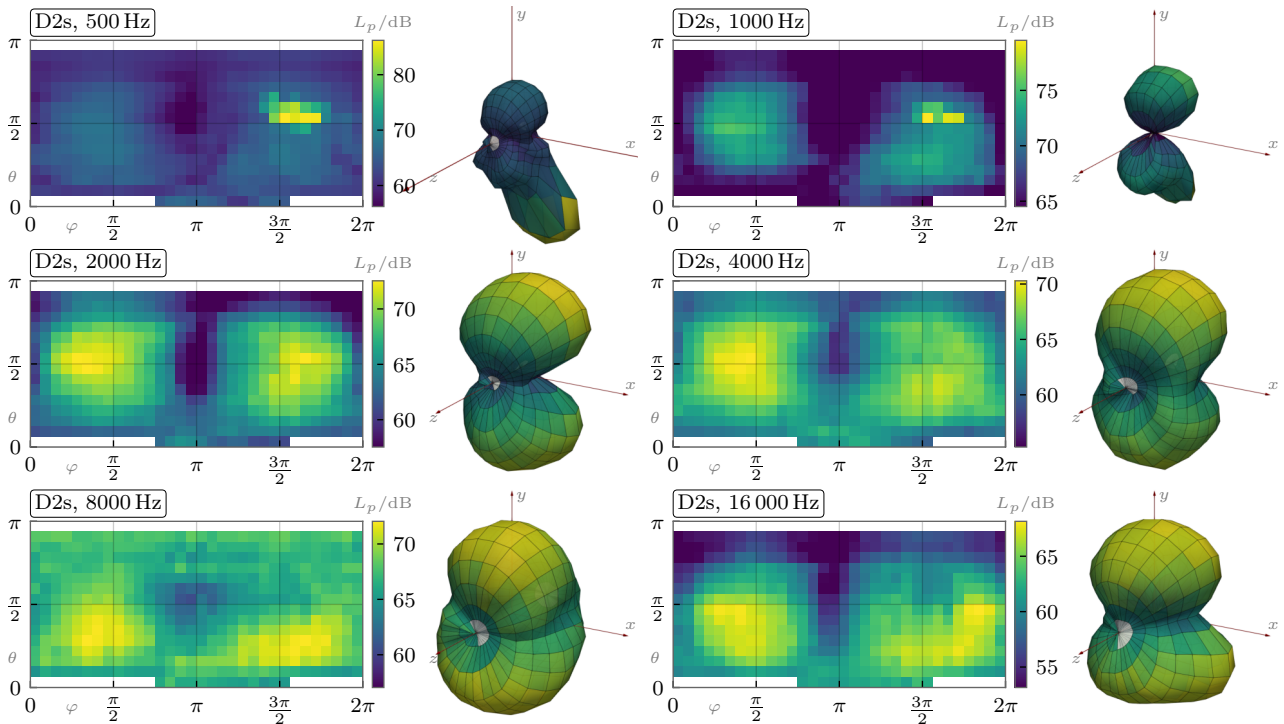
Figure 6: **D2s**: Directivity maps for different octave bands. Displayed dynamic up to 15 dB below maximum (except 500 Hz: 30 dB).
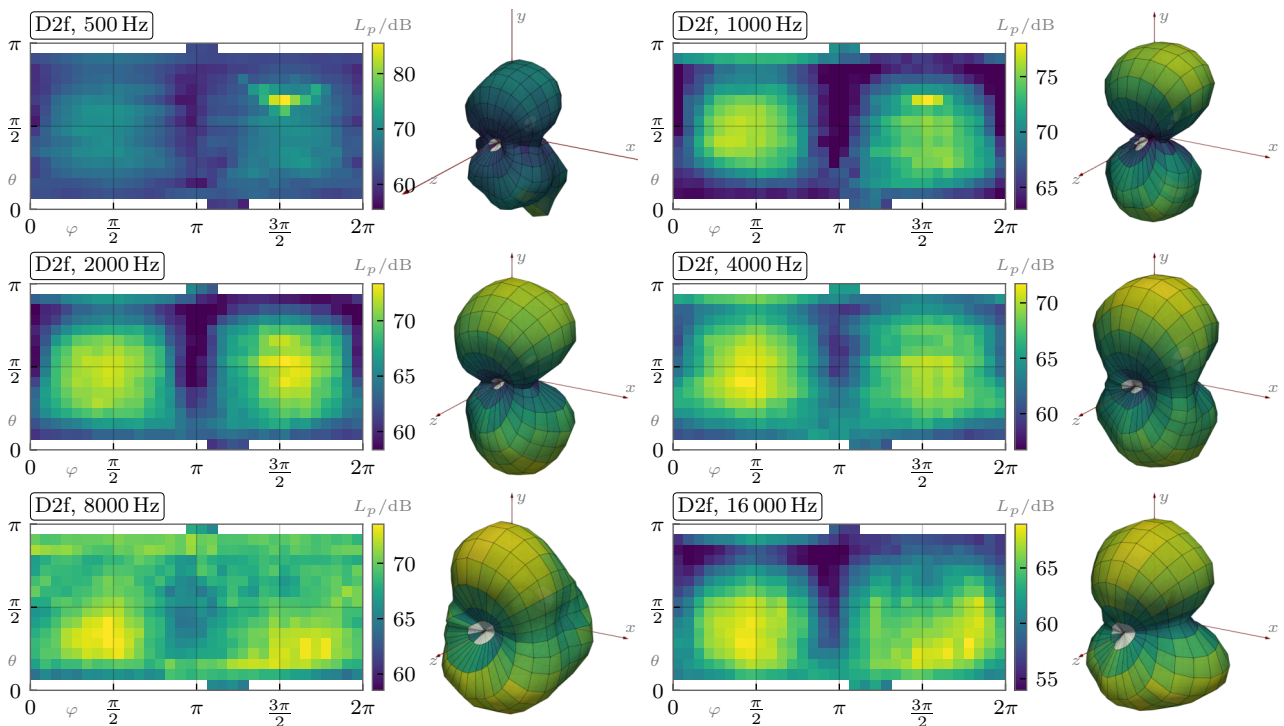

Figure 7: **D2f**: Directivity maps for different octave bands. Displayed dynamic up to 15 dB below maximum (except 500 Hz: 30 dB).
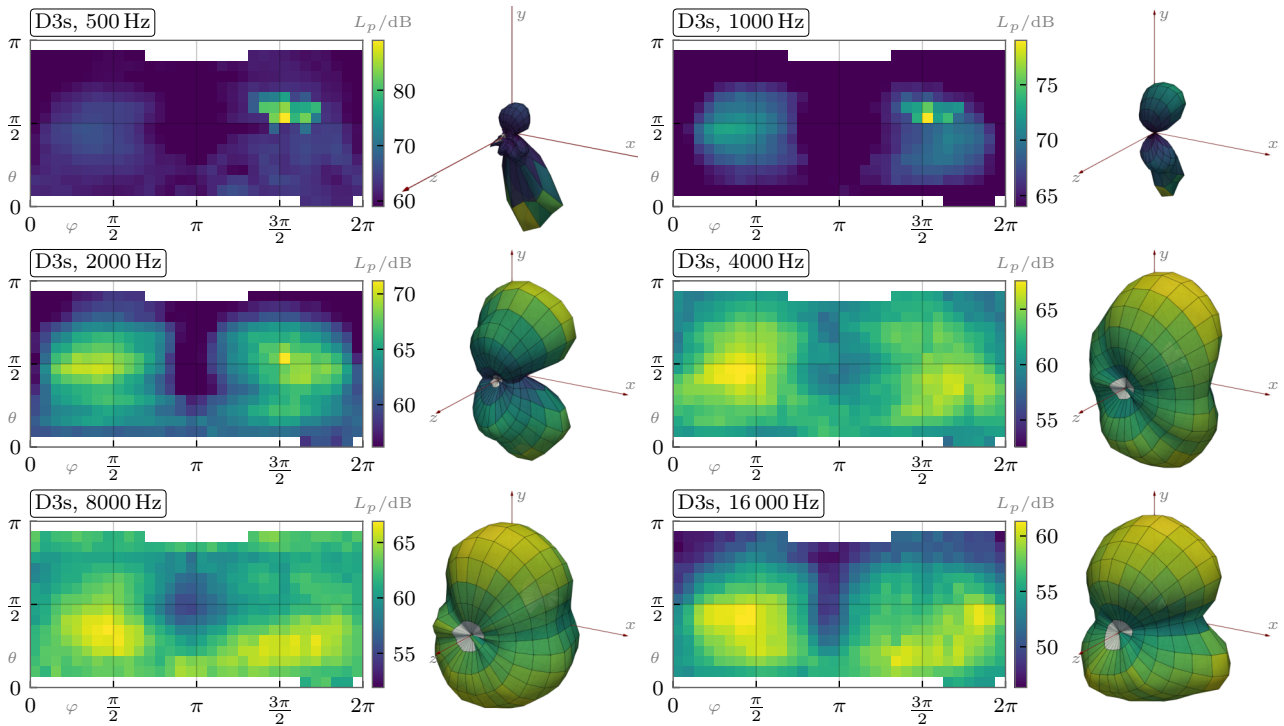
Figure 8: **D3s**: Directivity maps for different octave bands. Displayed dynamic up to 15 dB below maximum (except 500 Hz: 30 dB).
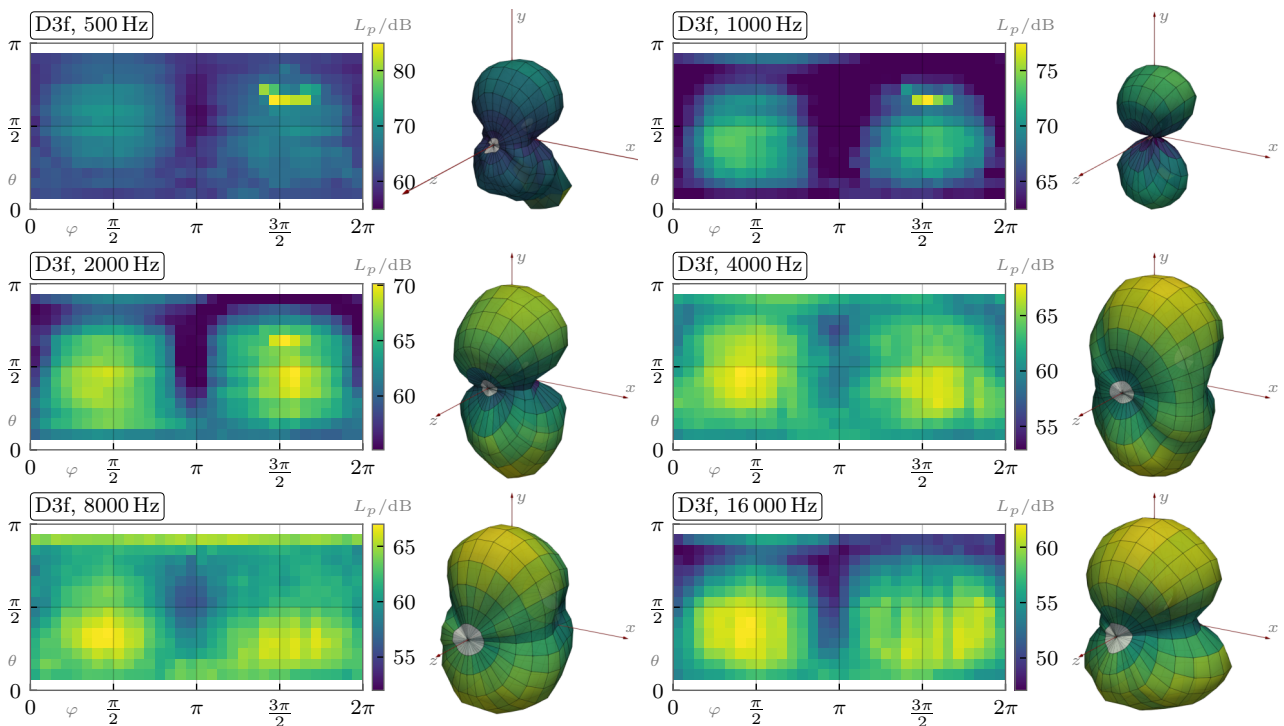

Figure 9: **D3f**: Directivity maps for different octave bands. Displayed dynamic up to 15 dB below maximum (except 500 Hz: 30 dB).

3.3 Sound power and directivity factor

Figure 10 shows the narrow-band sound power spectra, with the sound powers calculated according to Eq. (2). In the legend of the figures, the summed sound power levels (unweighted and A-weighted) are also documented. All spectra feature tonal and broadband components, with higher harmonics of the blade passing frequencies visible up to about 3 kHz and increased levels around 4 kHz.
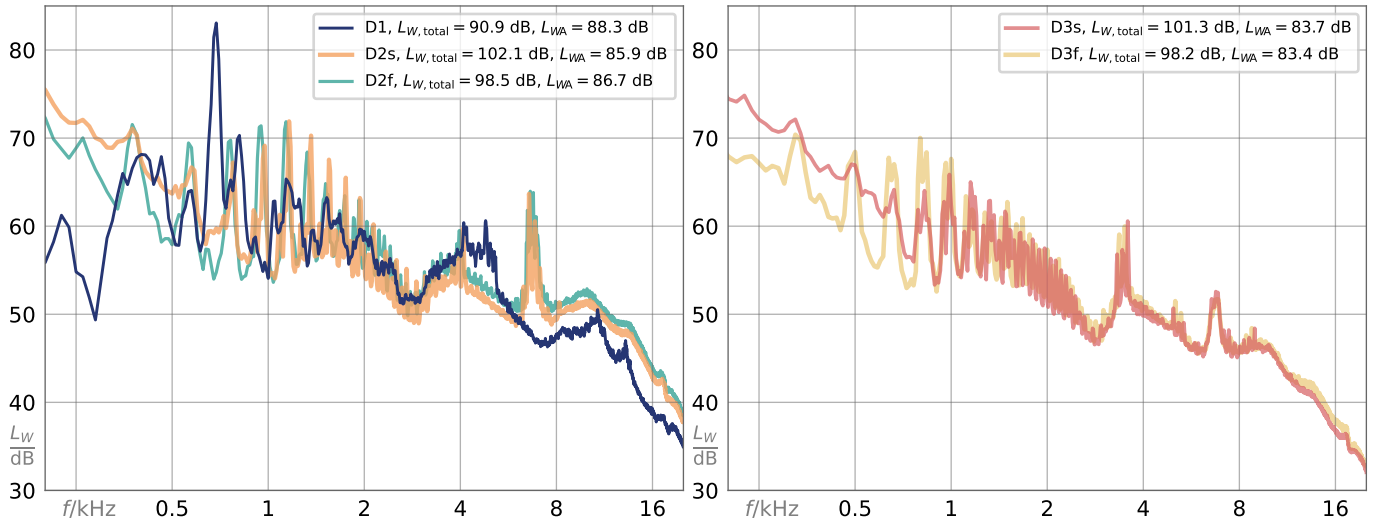

Figure 10: Narrow-band sound power spectra ($\Delta f = 12.5\,\text{Hz}$) of the drone flights.
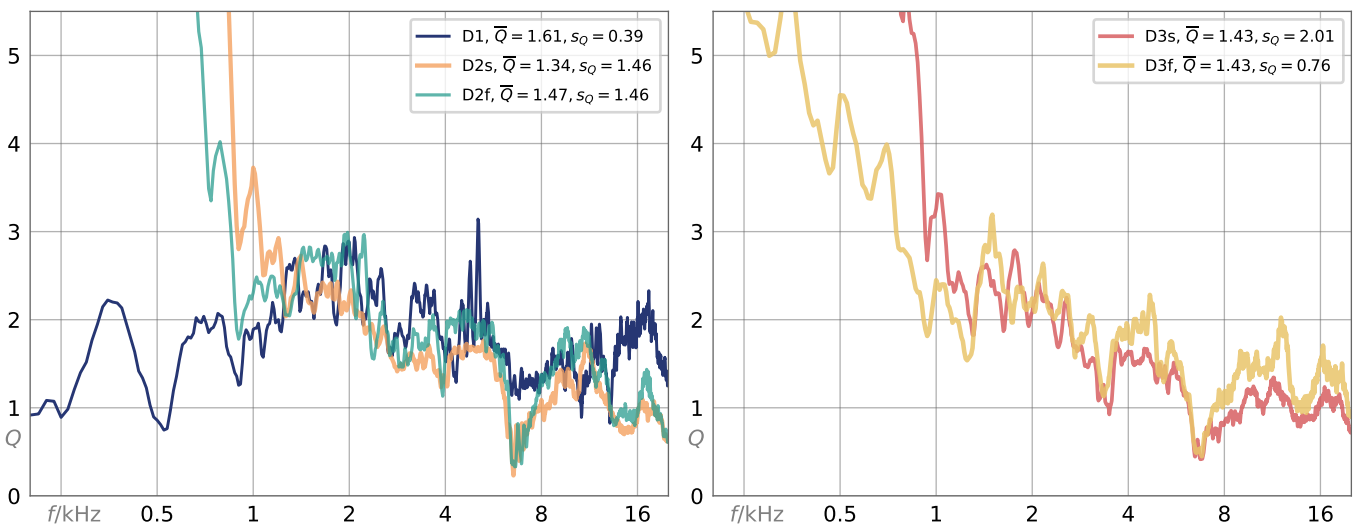

Figure 11: Frequency-dependent directivity factors of the drones (moving average over 10 adjacent frequencies, $\Delta f = 12.5\,\text{Hz}$).

The most prominent feature in the D1 spectrum is a tonal peak between 500 Hz and 1 kHz, which lies more the 10 dB above other parts of the spectrum. The D2 and D3 spectra have distinct tonal components as well, however, the energy is distributed more evenly over several of the blade passing frequency harmonics. In the D3 cases (with larger propeller diameters), the individual peaks are not as pronounced as in the D2 cases, and the overall level is also lower.

Comparing the spectra at higher frequencies shows that the faster moving cases (D2f/D3f) have slightly higher levels compared to the slow-moving drones. Between 1 kHz and 2 kHz, the tonal

components of D2s are increased compared to D2f, whereas D3s and D3f exhibit a similar characteristic in that frequency range. For frequencies below $500\,\mathrm{Hz}$, the broadband components appear to be significantly higher for the slow versus the fast drone flights. This is certainly due to the flow effects mentioned above, which can also be seen to have more impact in the directivity maps.

At $6.5\,\mathrm{kHz}$, the D2/D3 cases feature a strong tonal component which is not present in the D1 spectrum. Looking at the directivity spectrum (Fig. 11) at the same frequency, a minimum with $Q < 1$ can be seen. This means that in contrast to most of the spectrum, at this frequency more energy is radiated in other directions than downwards, which also hints at the underlying sound generating mechanism being a different one here.

The directivity factors of $Q \geq 3$ determined for $1\,\mathrm{kHz}$ and below for the D2 and D3 cases are not trustworthy, as the calculations, again, are biased by the pressure fluctuations due to flow over the sensors below the drone. A perfect monpole is characterized by a directivity factor of $Q_{\mathrm{monopole}} = 1$, for a dipole oriented along the y axis $Q_{\mathrm{dipole}} = 3$ [9]. As can be seen in Fig. 11, the results calculated for the drones between $1\,\mathrm{kHz}$ and $4\,\mathrm{kHz}$ hint at a radiation characteristic that lies between monopole and dipole for these frequencies.

4. Conclusion

A novel technique for reconstructing sound emission characteristics of drones in cruise flight mode has been successfully applied to several quadcopter drone fly-by measurements with a microphone array. For each measurement, the drone's directivity pattern was mapped. Moreover, the sound power spectrum and the frequency-dependent directivity factor were calculated.

While the general concept of the signal processing chain proved to be robust, the practical application to different configurations and scenarios uncovered several challenges to be overcome for future investigations:

1. For drones whose dimensions are non-negligible compared to the array, measures should be taken to ensure a sufficiently accurate tracking of the drone's center as reference position.

2. Techniques should be used to mitigate the effect of flow over microphones that may be in the wake of a propeller.

3. For mapping the directivity, the array geometry should be designed so as to uniformly sample all angles of interest over time.

4. The measuring environment should allow for the drones to be operated reproducibly in a representative flight mode.

Bearing these limitations in mind, the presented method has the potential to be a valuable tool for the in-flight characterization of the sound emission of drones.

References

[1] B. Schäffer, R. Pieren, K. Heutschi, J. M. Wunderli, and S. Becker, "Drone noise emission characteristics and noise effects on humans—a systematic review," *International Journal of Environmental Research and Public Health*, vol. 18, no. 11, 2021. DOI: `10.3390/ijerph18115940`.

[2] The European Commission, "Commission Delegated Regulation (EU) 2019/945 of 12 March 2019 on unmanned aircraft systems and on third-country operators of unmanned aircraft systems," Official Journal of the European Union L152, vol. 62, p. 1, 11 June 2019 2019.

[3] ISO, *ISO 3744:2010 – Acoustics – Determination of sound power levels and sound energy levels of noise sources using sound pressure – Engineering methods for an essentially free field over a reflecting plane*, 2010.

[4] G. Herold, "In-flight directivity and sound power measurement of small-scale unmanned aerial systems," preprint, 2022. DOI: `10.36227/techrxiv.19469825`.

[5] R. P. Dougherty, "Functional beamforming," in *Proceedings of the 5th Berlin Beamforming Conference*, Berlin, 2014, pp. 1–25.

[6] E. Sarradj and G. Herold, "A Python framework for microphone array data processing," *Applied Acoustics*, vol. 116, pp. 50–58, 2017. DOI: `10.1016/j.apacoust.2016.09.015`.

[7] B. D. O. Anderson and J. B. Moore, *Optimal filtering*. Englewood Cliffs, N.J.: Prentice-Hall, 1979, 357 pp.

[8] G. Herold, A. Kujawski, C. Strümpfel, S. Huschbeck, M. Uijt de Haag, and E. Sarradj, "Flight path tracking and acoustic signature separation of swarm quadcopter drones using microphone array measurements," in *Quiet Drones 2020 - International e-Symposium on UAV / UAS Noise*, Paris, France, 2020, pp. 1–19. DOI: `10.5281/zenodo.4548251`.

[9] L. L. Beranek and T. J. Mellow, *Acoustics: Sound fields and transducers*. Elsevier, 2012. DOI: `10.1016/B978-0-12-391421-7.00001-4`.